CILAMCE 2017
Florianópolis - Santa Catarina - Brazil

A COUPLED DISCRETE ELEMENT METHOD AND FINITE VOLUME METHOD FOR THE SIMULATION OF ELASTIC BODIES

Paolo Sassi

Jorge Freira

Mariana Mendina

Martn Draper

Gabriel Usera

gusera@fing.edu.uy

IMFIA, School of Engineering, UdelaR

Julio Herrera y Reissig , 11100, Montevideo, Uruguay

Abstract. *There are a wide variety of flexible and elastic systems that interact dynamically with fluids, usually water or air. These interactions involve a double complexity of the dynamics, as the systems go through large deformations due to the flow actions, and at the same time, the adopted configuration of the systems determines the flow responses. The design and analysis of the efficiency that these devices may have under different flow conditions can be carried out using numerical modeling tools. Devising ways of simulating the behavior of fluids with accuracy is essential to save time and resources while testing new technologies, especially in the generation of energy from renewable sources. The present research adapts mathematical methods, still new to the field, to represent flows of fluid in bidirectional interactions with new technologies, and particularly applies them to a new kind of vertical blade-less turbine that gathers energy from the vortex induced vibrations (VIV). This device has not yet been tested under rigorous theoretical models or with simulation methods that can have true predictive value. This research presents a framework for such modeling by coupling the discrete element method (DEM), with the Immersed Boundary Method (IBM), and the finite volume method (FVM).*

Keywords: *Computational Fluid Dynamics, ; Discrete Element Method, Finite Volume Method, Vorticity Wind Turbines, Immersed Boundary Method*

CILAMCE 2017
Proceedings of the XXXVIII Iberian Latin-American Congress on Computational Methods in Engineering
P.O. Faria, R.H. Lopez, L.F.F. Miguel, W.J.S. Gomes, M. Noronha (Editors), ABMEC, Florianpolis, SC, Brazil,
November 5-8, 2017

1 INTRODUCTION

In recent decades, renewable energies had a great deal of expansion. The causes for this growth are varied and can be associated with several changes, such as:

- A rise in environmental awareness and related policies, as there is currently a strong global pressure to slow down global warming with international commitments to reduce emissions by setting targets and maximum agreed levels;
- An expected depletion of the natural resources currently used for power generation, such as coal and gas;
- The widespread adoption of new generation technologies that are gaining ground in the global market and consolidating their position in the mainstream;
- The technological advancement of classic renewable generation (traditional wind-turbines and solar panels) that have gained performance;
- A growing tendency to diversify the energy matrix in order to avoid dependence on highly fluctuating fossil markets;
- An increment in energy demand, due to the rise of emergent economies;
- A need for isolated generation in rural areas, away from transmission lines, and even for micro-generation in urban areas.

Although there have been many substantial technical developments on large-scale wind generation, there are still no technologies with the same positive impact on the economic equation at the micro-generation level, either because of the long pay-back periods that small wind turbines involve or due to the susceptibility of these to the turbulence. So, it is unusual to find this type of installations either in urban or rural environments, as small scale wind infrastructures are less convenient than micro-generation installations of solar power.

The present research describes and analyzes numerically the generation of electric energy by transforming the kinetic energy of an oscillating structure, induced by the vortex detachment as it is immersed in a fluid flow, commonly known as VIV (Vortex Induced Vibrations). The structure to be analyzed is an inverted vertical cone coupled at the bottom to an elastic bar to which it is anchored, while it leaves the other end free to oscillate. The alternating detachment of the vortices over each side of the cone generates forces in a direction perpendicular to that of the stream flow, with equal frequency as the vortex shedding. These forces generate an angular oscillation of the whole structure, with respect to the anchor point of the elastic rod, which is maximized when the vortex detachment comes into resonance with the natural frequency of the structure.

The generation of electrical power through VIV has proven to be a very promising technology. In this scenario, it could certainly be very useful to have a tool capable of simulating the operation of these devices in order to contribute to their design and optimization by measuring their power output, resistance, durability, etc.

On the other hand, the recent increase in the processing power of computers and the development of parallel computation have allowed to devise numerical models suitable for a more accurate simulation and resolution of flows. In particular, computational fluid dynamics (CFD) codes play a crucial role, solving the flow around obstacles and allowing to capture the state of a certain specific situation. It is not surprising that the most advanced research projects use CFD tools to achieve advances in a wide variety of subjects, with applications ranging from macro frames of reference for climate studies to micro-scales in the study of blood flows, among many others. An accurate simulation may be a rather convenient way of producing useful data, mainly because of how cost-effective it is when compared with experiments performed in real environments. As the role of CFD is being expanded, new applications will arise that will demand new methodologies of simulation.

The discrete element method (DEM) is well suited to represent both loosely elastic structures and flexible bodies, while the finite volume method (FVM) is widely used to simulate fluid flow. In the last two decades, several open source fluid flow solvers have been made available under different grid topologies, ranging from fully structured all the way up to fully unstructured. Greater geometrical flexibility has been addressed also through the adoption of methods like immersed boundary methods (IBM) or local grid refinement.

2 LITERATURE REVIEW

2.1 Vortex Induced Vibrations

There are many research publications that numerically predict the motion of structural VIV, most of them studying circular cylinders immersed in flowing fluids. One of the first publications about VIV response of a cylinder was written by Parkinson (1972). He considered a mass, spring and dash-pot system driven by the fluid force resulting from vortex shedding. Equation (1) is the differential equation for transverse displacement (y) of a bluff body:

$$m\ddot{y} + c\dot{y} + ky = F_y = C_y \frac{1}{2} \rho_f V^2 D \tag{1}$$

where m = total oscillating structural mass; c = structural damping; k = spring constant; F_y = fluid force in the transverse direction; and the dot symbol stands for differentiation with respect to physical time t. Parkinson made two important assumptions in his research, the first being that the force and response are sinusoidal with the same frequency (f) and secondly that the fluid force leads the response by a constant phase angle Φ, this is the so-called lock-in effect,

$$F_y(t) = F_{y_o} \sin(\omega t + \Phi) \tag{2}$$

$$y(t) = A \sin(\omega t) \tag{3}$$

where $\omega = 2\pi f$; f = oscillation frequency; F_{yo} = amplitude of transverse force; and A = amplitude of the oscillation. With these considerations and applying it to a flexible cylinder he obtained relations for the vibration amplitude ($A^* = A/D$), Eq. (4), and frequency ($f^* = f/f_N$, with f_N = natural frequency), Eq. (5), as functions of the previous parameters, where the importance of the phase angle and the role played by mass and damping (mass-damping parameter, $\alpha = (m^* + C_A) \cdot \xi$) was shown very clearly.

$$A^* = \frac{1}{4\pi^3} \frac{C_y \sin(\Phi)}{(m^* + C_A)\xi} \left(\frac{U^*}{f^*}\right)^2 f^* \tag{4}$$

$$f^* = \sqrt{\frac{m^* + C_A}{m^* + C_{EA}}} \tag{5}$$

Here $U^* = U_o/(f \cdot D)$ is the reduced velocity; $m^* = \rho_m/\rho_f$ the ratio between the structure and the fluid densities; C_A is the potential flow added mass coefficient; and C_{EA} is an "effective" added mass coefficient that includes an apparent effect due to the total transverse fluid force in phase with the body acceleration.

Since the research by Parkinson, several other studies have emerged that analyze changes induced in the response of a cylinder under VIV by varying the parameters previously described. Griffin et al. (1975) made the so-called "Griffin plot", where the maximum VIV amplitude was plotted against the Shop-Griffin parameter, $S_G = 2\pi^3\ St^2\ (m^*\xi)$, and it was believed for some time that the amplitude of the VIV is insensitive to Reynolds number changes. However, Klamo et al. (2005) and Govardhan and Williamson (2006) have both since demonstrated the strong influence of the Reynolds number on the maximum VIV amplitude of a cylinder, and in the latter it is proposed that the amplitude is given by $A^* = g(\alpha) \cdot f(Re)$ presented in Eq. (6). Refer to Williamson and Govardhan (2008); Bearman (2011) for more detailed reviews.

$$A^* = \left(1 - 1.12\,\alpha + 0.30\,\alpha^2\right) \log\left(0.41\ Re^{0.36}\right) \tag{6}$$

2.2 Harvesting Energy from VIV

Whilst the norm is to avoid such synchronization regimes (ie. analyzing the effect on buildings, bridges, etc.), the aim of this research is to examine the opposite: finding ways of promoting the vortex-induced vibrations of a body in fluid flows, intending to facilitate energy production, that could be produced if the oscillation of the cylinder periodically displaces a magnet inside a coil. The energy production device will induce a structural damping term in the equation governing the motion of the cylinder, the underlying idea being that the energy dissipated by structural damping is at disposal to be harvested.

There are already many works aimed at the conversion of hydro-kinetic energy into a usable form of energy by enhancing the VIV of cylinders. Bernitsas et al. (2008b,a) introduce the Vortex Induced Vibrations Aquatic Clean Energy (VIVACE) converter, where a rigid VIVACE cylinder at high damping and Reynolds number is placed with its axis in the $z-$direction perpendicular to the flow velocity U, which is in the $x-$direction. The cylinder oscillates in the $y-$direction, which is perpendicular to its axis in z and the flow velocity in x. The research presents the experimental results from a laboratory rig where a variable electrical load resistance was connected to optimize the harnessed energy, reaching an integrated power efficiency of $\eta_{vivace} = 0.22$ and a peak of $\eta_{peak} = 0.31$.

Barrero-Gil et al. (2012) made a mathematical study parametric in the mass ratio (m^*) and the mechanical damping (ξ) parameters, to quantify the energy conversion. The expression for the efficiency is given by Eq. (7), and taking experimental data from forced vibrations tests, they conclude that: (i) the efficiency is mainly influenced by the mass-damping parameter and that there is an optimum value that maximize the efficiency; (ii) the range of reduced velocities with significant efficiency is mainly governed by m^*; and (iii) high efficiency values can be achieved for high Reynolds number, $\eta = 0.24$ was achieved for $m^*\xi = 0.35$ at $Re = 10,000$.

$$\eta = \pi A^*\, C_Y \sin \varPhi \left(\frac{f^*}{U^*}\right) \tag{7}$$

In a recent publication, Soti et al. (2017) explores numerically the generation of electrical power from VIV on a cylinder. In their work, the cylinder is free to oscillate in the transverse direction, attached to a magnet that can move along the axis of a coil made from conducting wire. The magnet and coil constitute a basic electrical generator and, according to Faraday's law of electromagnetic induction, the motion of the magnet produces a emf (ϵ) across the coil. If the coil is connected to a resistive load, an induced current will counteract the motion of the magnet by applying electromagnetic force.

For the calculation of the electromagnetic force they use the single magnetic dipole approximation proposed by Donoso et al. (2010) that includes a mathematical model of the interaction between a $N - turns$ coil and a single oscillating magnet. A set of experiments that validates the theoretical model of the oscillator are also presented and discussed in the publication. The magnetic force opposing the movement of the magnet is provided by Eq. (8) where $c_{m0} = \mu_m^2/(RD^4)$ is a constant (μ_m = magnetic moment of the magnet; R = resistive load; and D = diameter of the oscillating cylinder). And $g = g(y(t))$ is a function of the dimensions of the coil and its distance to the magnet, provided in Eq. (9).

$$F_m = c_{m0} g^2 \dot{y} \tag{8}$$

$$g(y) = \frac{2\pi N a^2}{L}\left[\frac{1}{\left(a^2 + (y_{cm} - L/2)^2\right)^{3/2}} - \frac{1}{\left(a^2 + (y_{cm} + L/2)^2\right)^{3/2}}\right] \tag{9}$$

where y_{cm} = the distance between the magnet and the coil; a = diameter of the coil; L = length of the coil. The magnetic force can be considered as a damping force with a non-constant damping coefficient $c_m = c_{m0}g^2$. The electrical power is calculated by multiplying the electromagnetic force with the velocity of the magnet $P(t) = F_m\dot{y}$. Lastly the efficiency is defined as the ratio of the electrical power to the power available over the fluid region occupied by the cylinder (not considering the amplitude of the oscillation). Several results are presented comparing constant versus electro-magnetic damping ratio, varying the coil length, coil radius, mass ratio, Reynolds number and finally using two coils. In all cases a maximum average efficiency of $\eta = 0.13$ was obtained.

2.3 Computational Fluid Dynamics, CFD

In the last two decades several open source fluid flow solvers have been made available Zaleski (2001), under different grid topologies ranging from fully structured, either orthogonal or not Lehnhuser and Schfer (2003), through block-structured grids Lilek et al. (1997), and up to fully unstructured. Greater geometrical flexibility has been addressed also through the adoption of methods like local grid refinement Lange et al. (2002), and immersed boundary Liao et al. (2010); Mendina et al. (2014) atop the underlying grids. A detailed review of this last method, originally introduced by Peskin Peskin (1982), is given in Mittal and Iaccarino (2005a).

The Discrete Element Method (DEM) is well suited to represent freely moving bodies and loosely elastic structures, while the Finite Volume Method (FVM) is widely used to simulate fluid flow Ferziger and Peric (2002); Lehnhuser and Schfer (2002). In this work we present a coupled model where a simple DEM method is implemented to represent the elastic rod, while the fluid flow is solved using caffa3d.MBRi Usera et al. (2008); Mendina et al. (2014) an open source fully implicit finite volume method for the 3D incompressible Navier-Stokes equations in complex geometry. Validation of the flow solver as well as mesh and time independence studies can be found in the given references.

Immersed Boundary Method, IBM

The immersed boundary method is a natural alternative to body-fitted or unstructured-grid methods when the aim is to simulate flow in domains with complex rigid boundaries, such as in fluid-solid interaction problems, which generally results in larger requirements of memory and involves higher computational costs. This demand is not only increased by the requiring transient re-meshing strategies that further raises the computational overhead and algorithmic complexity of these approaches, but also because, as the grid gets deformed, it gets harder to maintain the efficiency in solving the associated governing equations discretized in the Cartesian grid.

The IBM not only has the advantage of keeping the structured Cartesian grids but also provides the possibility to handle more complex geometries. The method was first implemented by Peskin (1972), and then generalized in Peskin (2002), who replaced the boundary by a field force which is defined on the mesh points of the rectangular domain and which is calculated from the configuration of the boundary.

In an IBM the Navier-Stokes equations are discretized on a Cartesian grid and the boundary condition would be imposed indirectly through the modification of the momentum and continuity equations. In general, the modification takes the form of a source term (or forcing function, f_b) in the governing equations, that reproduces the effect of the boundary. These implementations can be performed in two different ways. The continuous forcing is characterized by including the forcing function into the continuous governing equations. This leads to two different forcing functions ($f_b = (f_m, f_p)$), one that deals with the momentum and the other one with the pressure. The equations are then discretized in a Cartesian grid.

The second approach was proposed by Mohd-Yusof (1998), and it is commonly referred to as direct forcing or discrete forcing approach. Here the governing equations are first discretized on the Cartesian grid and then a forcing term (body force) is added in the source term, corresponding to the cells near the immersed boundary, in such a way that secures that the desired velocity distribution is satisfied at the boundary. This approach is sensitive to the discretization method. However, it provides easier control over numerical accuracy, stability and conservation properties of the solver. This approach was further extended by Fadlun et al. (2000), to reach a finite-difference formulation, where direct forcing was applied at the first Eulerian grid points external to the immersed boundary. Refer to Mittal and Iaccarino (2005b) for a further review and examples of the two approaches.

In the current work, the immersed boundary method is used, which it was already incorporated in caffa3d.MBRi. Refer to Mendina et al. (2014) for research that validates the method.

Discrete Element Method, DEM

The DEM is used for many kinds of applications. It is a numerical method for computing the motion and effects of a large number of small particles. As soon as computers became available, they started to be used for running physical simulations of the behavior of particles. With the advances in computing power and the development of numerical algorithms, it has become increasingly possible to numerically simulate millions of particles on a single processor.

The DEM was first used in applied physics for the modeling of plasma, semiconductors, liquids and phase-change simulations. A precondition for using the method is that the system to be represented should be rightfully interpreted as an assembly of objects, and the laws governing their interaction must be known in order to obtain results that could be consistent with reality. The early evolution of the method, as well as the theory and computational aspects of particle simulations are described in Hockney and Eastwood (1988).

Today DEM has become widely accepted as an effective method for addressing engineering problems in granular and discontinuous materials, especially in granular flows, powder mechanics, and rock mechanics, since the studies by Cundall and Strack (1979). Nowadays its applications are being extended to analyze load and deformation on flexible and elastic systems in addition to the initial application for determining the failure of structures.

The general DEM is based on a double integration of the Newton equations of motion of each element. As the motion of an element is considered uncoupled from the motion of the rest of the elements during a time step, there is no need to assemble a stiffness matrix. Instead, coupling is obtained by updating the spring forces at every time step; each element will move, in the next step, due to the unbalance on the summation of forces in all springs attached to the element. Two types of damping are applied to reach equilibrium: the relative motion between elements of the structure is damped by a coefficient of damping calculated from the critical damping ratio of the material. Secondly, due to the motion of the structure immersed in fluid, there is a small amount of viscous damping, that represents the resistance of the medium in which the structure is placed.

Ivanov (2001), have developed a three-dimensional DEM program for the analysis of engineering structures subject to earthquake loads. A chapter of his Ph.D. thesis is devoted to the analysis of shell structures with the DEM. In his work, he represents the in-plane stiffness of shells by a lattice of energy equivalent normal springs, while the bending stiffness of walls is represented by bending springs. He considers the elements of the lattice as beams that can transfer normal forces, F^n (due to tension and compression stresses), shear forces F^s, and bending moment M. In the research presented by Ivanov, the DEM algorithm to analyze solids is described in detail and used for the analysis of the shell structure. In Section 3.3 that algorithm will be adjusted to represent the dynamics of the flexible rod of the Vorticity Wind Turbine, VWT.

3 MODELING

The VWT structure consists of four essential parts:

- **Foundation:** underground structure that adds stability to the turbine,
- **Generation system:** the kinetic energy from the oscillations is converted into electricity by a built-in linear alternator,
- **Rod:** made of carbon fiber, it provides strength and flexibility to the movement, while minimizing energy dissipation and providing the highest resistance to fatigue. It penetrates into the mast for 20 percent of the mast length, is anchored to it at its top end and the bottom is secured to the foundation,
- **Mast:** light conic structure built using resins reinforced with carbon and glass fiber that

oscillates. It is designed to be substantially rigid, remaining anchored to the rod at its bottom. The top is unconstrained and presents the maximum amplitude of the oscillation.

3.1 Computational domain

The strategy to analyze the VWT structure is to divide it in two main parts, the rod and the mast, and treat the forces acting over these parts separately. The rod is analyzed as a beam anchored vertically to the ground with the DEM method, while the mast is represented by the Immersed Boundary Method.

The domain for the simulations is presented as a prism of $(8 \times 6 \times 15)$ meters in the $(x, y$ and $z)$ directions respectively. It is divided in cubic cells of $5\,cm$ side distributed in four blocks and regions of $(2 \times 6 \times 15)$ meters, one block for each region, named as blocks I, II, III and IV from west to east (x direction). The western block of the domain, block I, has inlet boundary condition where a uniform flow of $U_o = 9.1\,m/s$ in the x direction enters to the domain by its west boundary, the east boundary of this block has interface boundary conditions as the middle blocks, II and III, in their west and east boundaries and the eastern block, IV, in its west boundary. Block IV, has null-gradient outlet boundary condition in its east boundary. All, north, south, top and bottom boundaries of the four blocks have non-slip walls boundary conditions.

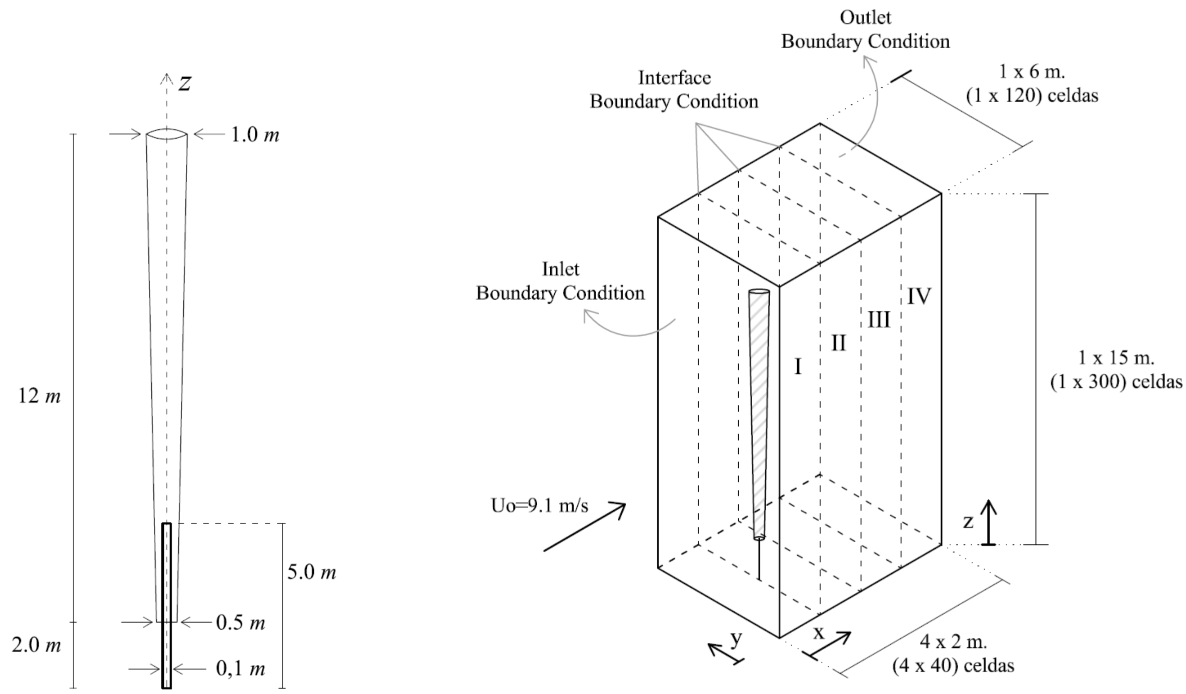

(a) Scheme of the generator system

(b) Computational Domain

Figure 1: Scheme of the Vorticity Wind Turbine and Computational Domain

A processor is used for each region, and so four processors (Xeon E5 family at Cluster-fing) are used for the simulations with Message Passing Interface (MPI), parallel computing. Thus, the whole domain consists of $(160 \times 120 \times 300)$ cells adding a total of 5,760,000 cells, 1,440,000 computed in each processor. The time step for the fluid flow solver is set at $dt = 0.01\,sec$ and for computing 1 second of simulation time it takes almost one hours of computing time.

3.2 Mast

The mast is an inverted cone as shown in Fig. 1a, represented as a rigid structure with the direct forcing approach of the IBM introduced in Section 2.3. It is represented mathematically at each time step as a function of the position and normal direction of the last element of the rod (described in Section 3.3).

The source term corresponding to the cells inside of the mast, is modified to make the velocity of each cell equal to the translational velocity of the mast. This is equivalent to adding a mass field $\vec{F^*}$ in the inner cells. Integrating this field in a closed region (D) surrounding the mast, the force that the body exerts over the fluid is obtained, and so:

$$F_{imb} = -\int_D \rho\,\vec{F^*}\,dV \tag{10}$$

the same can be applied to calculate the moment that the overall force exerts over the connecting node (*CN*) of the elastic rod, the highest node of the rod, where the mast and the rod are connected.

$$M_{imb} = -\int_D (P-O)\wedge(\rho\,\vec{F^*})\,dV \tag{11}$$

Where $(P-O)$ is the distance from every computing point from the region (D) to the connecting node. Once the force that the fluid exerts over the mast (F_{imb}) and the moment with respect to the connecting node (M_{imb}) are calculated, the procedure continues with the analysis of the rod.

3.3 Rod

The rod is the main section for the modeling of the structure because of its flexibility and elasticity. It is constructed with the DEM approach proposed by Ivanov (2001), composed of 20 equal bars of length $l = 10\,cm$ and diameter $D_{rod} = 10\,cm$, that conform the 2 meters rod (L_{rod}), see Fig. 2a. Note that, as the mast is modeled with IBM as a rigid body, there is no bending taking place in the part of the rod that penetrates into the mast, and for that reason only the first two meters of the rod have to be modeled. Each bar is constructed as a linear bar with two punctual nodes, sharing with the next bar one of those punctual nodes at each end, schematic representation in Fig. 3b. The nodes are the contact points in which the forces and moments are transmitted from bar to bar. Figure 3 shows the schematic representation of forces in Fig. 3a and the corresponding deformations in Fig. 3b, the bar is named with a counter "i" (from 1 to 20) and the nodes are numbered for each bar "i_1" and "i_2". The external forces, and moment are applied in the highest node, named as "Connecting-Node" (CN) because is the one that connects the rod and the mast.

Update of velocities

The motion of each element of the rod is represented by the first and second cardinal equations, applied at the center of the bars and used to calculate the displacement and rotation of the contact nodes (endings). The first, Eq. (12), is the equation for translational motion, and the second for rotational motion, Eq. (13), of a single bar "i".

$$\ddot{x}_i + \alpha\,\dot{x}_i = \frac{F_i}{m_i} + g \tag{12}$$

$$\dot{\omega}_i + \alpha\,\omega_i = \frac{M_i}{I_i} \tag{13}$$

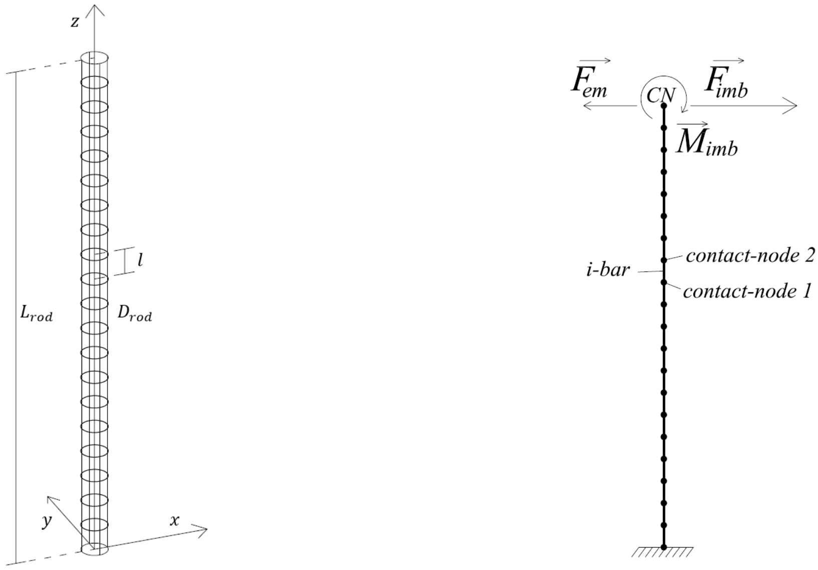

(a) Rod DEM Scheme

(b) Scheme of the modeling of the rod with the immersed boundary force and moment, and the magnetic force applied over the connecting node.

Figure 2: Modeling of the Rod

Figure 3: Forces and the corresponding deformations of the bars

where x_i = position vector; ω_i = rotational velocity; m_i = mass; I_i = mass moment of inertia; and g = gravity acceleration. The dots represent the derivative in time. A centered finite difference is used for the integration of the equations of motion. New and old values, within a time step, are designated by superscripts plus and minus respectively, thus the expression for translational and rotational velocities are provided by

$$\dot{x}_i = \frac{1}{2}\left[\dot{x}_i^- + \dot{x}_i^+\right] \tag{14}$$

$$\omega_i = \frac{1}{2}\left[\omega_i^- + \omega_i^+\right] \tag{15}$$

and the expression for translational and rotational accelerations,

$$\ddot{x}_i = \frac{1}{\Delta t_{dem}}\left[\dot{x}_i^+ - \dot{x}_i^-\right] \tag{16}$$

$$\dot{\omega}_i = \frac{1}{\Delta t_{dem}}\left[\omega_i^+ - \omega_i^-\right] \tag{17}$$

inserting this expressions in the equations of motion, Eq. (12) and Eq. (13), and solving for new values of velocities results in:

$$\dot{x}_i^+ = \left[D_1\,\dot{x}_i^- + (\frac{F_i}{m_i} + g)\Delta t_{dem}\right] D_2 \tag{18}$$

$$\omega_i^+ = \left[D_1\,\omega_i^- + (\frac{M_i}{I_i})\Delta t_{dem}\right] D_2 \tag{19}$$

where $D_1 = 1 - (\alpha\,\Delta t_{dem}/2)$, and $D_2 = 1/[1 + (\alpha\,\Delta t_{dem}/2)]$, with Δt_{dem} = time step for the DEM. The time step used for the displacement of the rod is smaller than the time step used by the fluid solver (caffa3d.MBRi), as the differential equations system governing the motion of the rod is too stiff, because of the high Young's module of the material, and then it is necessary to use a smaller time step than the one required for solving the fluid. In the simulations presented in this work, for every time step of the fluid solver the DEM is executed 10,000 times in order to reach the convergence of the system.

Update of contact forces

With the new velocities obtained, it is possible to update the contact forces in the nodes in between bars, which depend on the properties of the system. In the following description, the contact between two consecutive bars i and j is considered, as outlined in Fig. 4. To update the normal and shear forces, and bending moment, first the incremental displacements of the contact point due to translational and rotational motions of the elements are computed using the new values of velocities. Note that for each bar there are two nodes (one at each end) denoted as 'i_1' and 'i_2' for bar i, and j_1 and j_2 for bar j. As the contact node $c = i_2 = j_1$ belongs to both bars, it has two displacements. One obtained computing on bar i, Δx_{ci} and the other from computing on bar j, Δx_{cj}. Eq. (20a) calculates the translational displacement for the contact node obtained by computing on both bars.

$$\Delta x_{ci}^{tr} = \dot{x}_i^+ \Delta t \qquad \Delta x_{cj}^{tr} = \dot{x}_j^+ \Delta t \tag{20a}$$

$$\Delta x_{ci}^{rot} = ic^+ \wedge \Delta\theta_i \qquad \Delta x_{cj}^{rot} = -jc^+ \wedge \Delta\theta_j \tag{20b}$$

where ic^+ and jc^+ are the current vectors from the center of the bar to the contact points, and $\Delta\theta_i$ and $\Delta\theta_j$ are the incremental rotation of the bars. For the first time step the method uses values of position and velocity provided as initial conditions. Thus, the total incremental displacement at the contact is:

$$\Delta x_c = (\Delta x_{cj}^{tr} - \Delta x_{ci}^{tr}) + (\Delta x_{ci}^{rot} - \Delta x_{cj}^{rot}) \tag{21}$$

which resolves into normal and shear components as:

$$\Delta x_c^n = (\Delta x_c\, n_{ij}^{+\,\prime})\, n_{ij}^+ \tag{22}$$

$$\Delta x_c^s = \Delta x_c - \Delta x_c^n \tag{23}$$

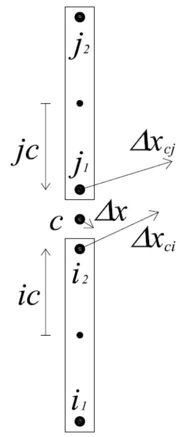

Figure 4: Scheme of the contact node

here n_{ij} is the unit normal vector pointing from bar "i" to bar "j"; the supra-index "$'$" stands for the transposed vector (so as to be able to calculate the product). And the angular displacements for bars "i" and "j" can be calculated as:

$$\Delta\theta_i = \omega_i^+ \,\Delta\, t, \qquad \Delta\theta_j = \omega_j^+ \,\Delta\, t \tag{24}$$

then, the increment of force in the normal spring is expressed in Eq. (25), where A_t = transversal area; E = Young's modulus; l = element length; and ν = Poisson's ratio (material property).

$$\Delta F_c^n = k_n \,\Delta x_c^n, \quad \text{with} \quad k_n = \frac{\sqrt{3}}{3}\,\frac{A_t\, E}{l(1-\nu)} \tag{25}$$

The calculation of the increments of the shear force and bending moment is not as simple as the normal force and further calculations are needed. The relation between these forces and the corresponding displacement for the endpoint i_1 of the bar 'i' with second moment of inertia I_i is expressed in Eq. (26) and Eq. (27),

$$F_{i_1}^s = \frac{12EI_i}{l^3}(x_{i1}^s - x_{i2}^s) - \frac{6EI_i}{l^2}(\theta_{i1} - \theta_{i2}) \tag{26}$$

$$M_{i1} = \frac{6EI_i}{l^2}(x_{i1}^s - x_{i2}^s) - \frac{4EI_i}{l}\big(\theta_{i1} - \frac{\theta_{i2}}{2}\big) \tag{27}$$

with symmetric relations for node i_2, where x = position vector and θ = rotation of the element, see Fig. 3b. An additional set of spring constants is defined accounting for the bending behavior equal to the coefficients of Eq. (26) and Eq. (27) as follows: $k_{qq} = 12EI/l^3$, $k_{qm} = k_{mq} = 6EI/l^2$ and $k_{mm} = 4EI/l$. Then the respective contributions to the driving force and driving moment are calculated as functions of the relative incremental shear displacement Δx_c^s, and the incremental rotations of the elements $\Delta\theta_{i1}$ and $\Delta\theta_{i2}$.

$$\Delta F_{i1}^s = -\Delta F_{i2}^s = k_{qq}\Delta x_c^s + k_{qm} \cdot n_{ij}^+ \wedge (\Delta\theta_{i1} + \Delta\theta_{i2}) \tag{28}$$

Before incrementing the values of the contact forces, their old directions have to be corrected in order to reflect the latest orientation of the contact plane. The old normal force should be modified to be collinear to the latest unit normal vector,

$$F_c^{n-} = (F_c^{n-}\, n_{ij}^{+}{}')n_{ij}^{+} \tag{29}$$

The shear contact force is first updated to be co-planar with the latest contact plane,

$$F_c^{s-} = a^{+}(a^{-}\, F_c^{s-}{}') + b\,(b\, F_c^{s-}{}') \tag{30}$$

where a^+, a^- and b are auxiliary unit vectors given by the expressions $b = (n_{ij}^- \times n_{ij}^+)/|(n_{ij}^- \times n_{ij}^+)|$; $a^- = b \times n_{ij}^-$ and $a^+ = b \times n_{ij}^+$. Finally, the rotation of the contact shear force has to be considered along the n_{ij} axis. The average rotation along this axis will be $\Delta\theta = 1/2 \cdot (\Delta\theta_{i1} + \Delta\theta_{i2}) \cdot n_{ij}^{+}{}'$. The final updated old shear contact force (co-planar with the new contact plane) will be,

$$F_c^{s-} = \cos(\Delta\theta)\, F_c^{s-} + \sin(\Delta\theta)(a^{+} \wedge F_c^{s-}) \tag{31}$$

once having corrected the direction of the old contact forces, the incremented ones will yield the new values, with $\Delta F_{i1}^n = -\Delta F_{i2}^n$ and $\Delta F_{i1}^s = -\Delta F_{i2}^s$,

$$F_{i1}^{n+} = F_{i1}^{n-} + \Delta F_{i1}^{n} \qquad F_{i2}^{n+} = F_{i2}^{n-} + \Delta F_{i2}^{n} \tag{32a}$$

$$F_{i1}^{s+} = F_{i1}^{s-} + \Delta F_{i1}^{s} \qquad F_{i2}^{s+} = F_{i2}^{s-} + \Delta F_{i2}^{s} \tag{32b}$$

Resuming Eq. (27), the increment of moments is computed as:

$$\Delta M_{i1} = k_{qm}\, n_{ij}^{+} \wedge \Delta x^s - k_{mm}\,(\Delta\theta_{i1} + \Delta\theta_{i2}/2) \tag{33}$$

$$\Delta M_{i2} = k_{qm}\, n_{ij}^{+} \wedge \Delta x^s - k_{mm}\,(\Delta\theta_{i2} + \Delta\theta_{i1}/2) \tag{34}$$

and the increment of the moment at both ends:

$$M_{i1}^{+} = M_{i1}^{-} + \Delta M_{i1}, \quad M_{i2}^{+} = M_{i2}^{-} + \Delta M_{i2} \tag{35}$$

Compute external forces

This iterative procedure is computed for every bar composing the rod. When computing on the highest bar, the force that the fluid exerts over the mast (F_{imb}) is transmitted to the connecting node (the one that is connected to the mast), as well as the moment with respect to this node (M_{imb}), calculated in the previous Section 3.2 with the IBM. It should be also considered at this stage the magnetic force that the generator exerts over the rod (F_{em}), as it is also applied to the connecting node, see Fig. 2b. In the next Section 3.4, it will be explained how that magnetic force should be calculated.

$$F_{CN}^{+} = F_{CN}^{-} + \Delta F_{CN} + F_{imb} + F_{em} \tag{36}$$

$$M_{CN}^{+} = M_{CN}^{-} + \Delta M_{CN} + M_{imb} \tag{37}$$

Having computed the stresses and moment resultants acting on each element, the system is ready to enter a new time step. It is worth highlighting that as the time step for this procedure is smaller than the one for solving the fluid equations, the same immersed boundary force and moment are used during several iterations until the fluid solver time step is advanced.

Table 1: Parameters used in the model of the generator

Property	Value	Unit
L_{coil}	7.0	cm
a_{coil}	5.0	cm
N_{coil}	700	turns
R_{load}	7	Ω
μ_m	4.5e-3	J/T
$y^0_{cm,1}$	-8.5	cm
$y^0_{cm,2}$	+8.5	cm

3.4 Linear Generator

The kinetic energy of the oscillations is converted into electricity using a linear built-in generator as the one described by Donoso et al. (2010). It is composed of a magnet coupled to the last bar of the rod, modeled as a punctual magnet, and two fixed coils, one at each side of the rod, see Fig. 5. When the system is oscillating, the magnet oscillates with the rod, generating an oscillating magnetic field inside the coils. According to Faraday's law of electromagnetic induction, the motion of the magnet produces emf (ϵ) across the coil. Connecting the coil to a resistive load, an induced current appears, opposing the motion of the magnet by applying an electromagnetic force (F_{em}), which can be considered as a damping force in the motion of the rod.

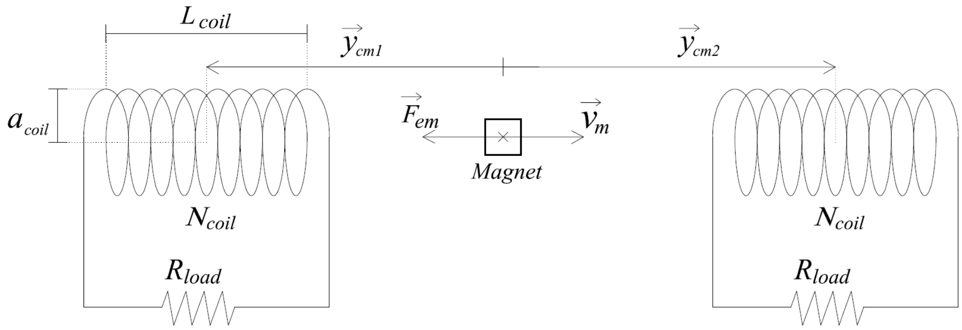

Figure 5: Scheme of the generator system

The magnetic force that each coil exerts over the magnet is a function of the magnet velocity and its relative position to the coils, as well as to the properties of the coils and the magnet, and the resistive load connected to each circuit. Here two identical coils are disposed at each side of the rod, connected to two identical loads for reaching a symmetrical displacement. In equilibrium conditions the center of the coils are located at 8.5 cm in $y-$ direction at each side of the magnet. The properties of the magnet and the coils are listed in Table 1.

From the literature, the equation of the magnetic force ($F_{em,i}$) is obtained as follows:

$$F_{em,i} = c_{m0}\, g_i^2\, \dot{y} \qquad \text{with} \qquad c_{m0} = \frac{\mu_m^2}{R} \tag{38}$$

where μ_m is the magnetic moment of the magnet. Here it is constant because the resistive load (R) is set to be constant, but it could be variable, for instance, within the wind velocity. $g_i(y)$ is a function of the relative position between the $i-$coil and the magnet ($y_{cm,i}$), expressed as:

$$g_i(y) = \frac{2\pi N_{coil} a_{coil}^2}{L_{coil}} \left[\frac{1}{\left(a_{coil}^2 + (y_{cm,i} - L_{coil}/2)^2\right)^{3/2}} - \frac{1}{\left(a_{coil}^2 + (y_{cm,i} + L_{coil}/2)^2\right)^{3/2}} \right] \tag{39}$$

where the properties of the coil, denoted with the subindex "$coil$", are illustrated in Fig. 5, together with the distance from the magnet to each coil, $y_{cm,i}$.

The magnetic forces are calculated at each time step of the DEM, added in a single force (F_{em}), and applied to the highest bar of the rod as expressed in Eq. 36. Note that the magnet is also modeled as a punctual element. As this force opposes the motion of the bar and it is proportional to its velocity, it can be interpreted as a damping force.

To calculate the output power, P, the electromagnetic force is multiplied by the magnet velocity at each time step, the negative value is because the force opposes the motion,

$$P(t) = -F_{em}\, v_{mg} \tag{40}$$

in this way, the output power is determinate just for an instant of time. Integrating the instantaneous power over a period of time T^*, the accumulated energy is obtained, and dividing then by the value of that period of time, the average output power, $\bar{P}$, is obtained:

$$\overline{P} = \frac{E_T}{T^*} = \frac{1}{T^*} \int_{T^*} P(t)\, dt \tag{41}$$

Finally, the efficiency of the VWT is defined as the ratio of the output power to the power available in the fluid flow over the region occupied by the turbine. The latter is constant in this simulations because an uniform flow is used. If dividing the instantaneous power, then the instantaneous efficiency is obtained, η; and the integrated efficiency, $\bar{\eta}$, is obtained dividing the integrated power:

$$\overline{\eta} = \frac{\overline{P}}{1/2\, \rho\, U^3 A_{sw}} \tag{42}$$

Where U is the velocity of the fluid flow upstream, and A_{sw} is the swept area by the oscillation of the VWT in a plane perpendicular to the flow direction.

4 RESULTS

The modeling of a vorticity wind turbine (VWT), as explained in the previous chapter, was carried through and simulated numerically with caffa3d.MBRi. Results are presented in this section, in a first instance, for a uniform air flow of $U_o = 9.1 \cdot m/s$, as this is the critical velocity, this mean that the vortex shedding frequency is equal to the natural frequency of the structure. The Reynolds number calculated at the equivalent height $h_e = 8.4\,m$ (60 % of the mast height) for the critical velocity is $Re = 4.67\,E5$. Following that, a sensitivity analysis to wind speed and other relevant parameters will be shown.

Figure 6 shows the simulated VWT. The reduced velocity field is displayed in the $x-direction$ over the horizontal plane. The grey cone is the mast, represented by the IBM and the thin black line is the rod, represented by the structural DEM as a linear bar, invisible to the fluid. The vortex detachment can be seen in the velocity field.

Figure 6: Simulation

Figure 7 shows the reduced transversal displacement of the top of the rod ($y^* = y/D$ with D the diameter at the top of the mast), where the magnet is located, for a 30 second simulation with uniform air flow of $U_o = 9.1\,m/s$. The oscillatory response shows that the lock-in effect is well captured by the coupled simulation, and that the device is taking energy from the fluid. This is evidenced by the sinusoidal displacement, of amplitude $A = 0.15\,D$ (with D the diameter of the top of the mast), which correlates with the graph of the transversal displacement for structures under the lock-in effect. The response shows different frequencies, distinguishable from the slight difference between peaks and valleys presented in the figure, anyway the main oscillatory frequency of the turbine can be calculated from Fig. 7, $f = 1.258\,Hz$. Note that at the top of the mast, the amplitude of the oscillations are much wider. For the same simulation, the amplitude of the transversal displacement at the top of the mast is twice its diameter.

In order to be able to determine the frequency of the vortex shedding, the reduced in-plane vorticity, ω_k^*, defined in Eq. (43), is calculated in three monitoring points at every 0.01 seconds and plotted vs time in the upper panel of Fig. 8. The three monitoring points are set for the same

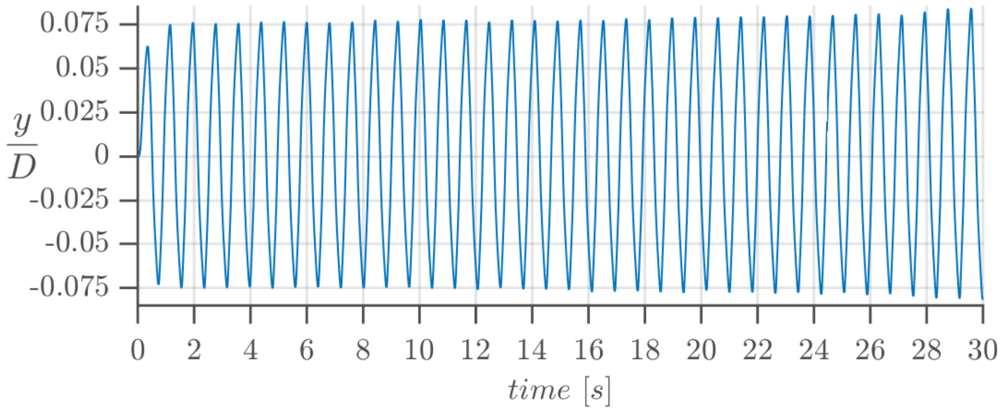

Figure 7: Dimensionless transversal displacement of the top of the rod, where the magnet is located.

x and y coordinate components, downstream the turbine, and at three different heights, z_1, z_2 and z_3 (corresponding to 20%, 50% and 80% of the height of the mast respectively). In the discretized domain, the two-dimensional vorticity is calculated with the least-square method in Eq. (44).

$$\omega_k = (\nabla \wedge \vec{v})\,\hat{k} \qquad \omega_k^* = \frac{\omega_k}{U_o/D} \tag{43}$$

$$\omega_k = -\frac{2\,v_{i+2,j} + v_{i+1,j} - v_{i-1,j} - 2\,v_{i-2,j}}{10\Delta x} + \frac{2\,u_{i,j+2} + u_{i,j+1} - u_{i,j-1} - 2,u_{i,j-2}}{10\Delta y} \tag{44}$$

Where i is the cell index of the $x - coordinate$ and j the cell index of the $y - coordinate$, u is the velocity component in $x - direction$ and v in $y - direction$, and Δx and Δy are the distance between two consecutive computing points in x and $y - direction$ respectively.

Two important concepts are drawn from the plotted data in the upper panel of Fig. 8. First of all, the frequency of the vortex shedding can be determined, $f_{vs} = 1.25 \cdot Hz$, and secondly it can be seen that the shedding is synchronized along the height of the mast. Because of this, the transversal force integrated along the structure, at a given instant of time, will be maximized. Otherwise, opposing forces will coexist along the structure, and the resulting force will be reduced. The bottom panel plots the integrated transversal force acting over the mast, divided by $\rho(UD)^2$. Here the frequency of the force can be obtained and compared with the vortex shedding frequency, which turn out to be the same, as expected. In order to verify the dynamics of the oscillation, the Strouhal number and the Reynolds number at the top of the VWT have been calculated. The red dot in Fig. 9 represents the working point of the simulation, and the black line, taken from the literature, is the Struhal number as a funcion of the Reynolds number for cylinders.

To quantitatively assess the output energy production, the calculations of Section 3.4 were followed. In Figure 10 three plots are shown: the upper panel plots the reduced velocity of the last element of the rod (where the magnet is fixed, and thus this velocity is equal to the magnet velocity) during 10 seconds of the simulation. The mid panel plots the reduced magnetic

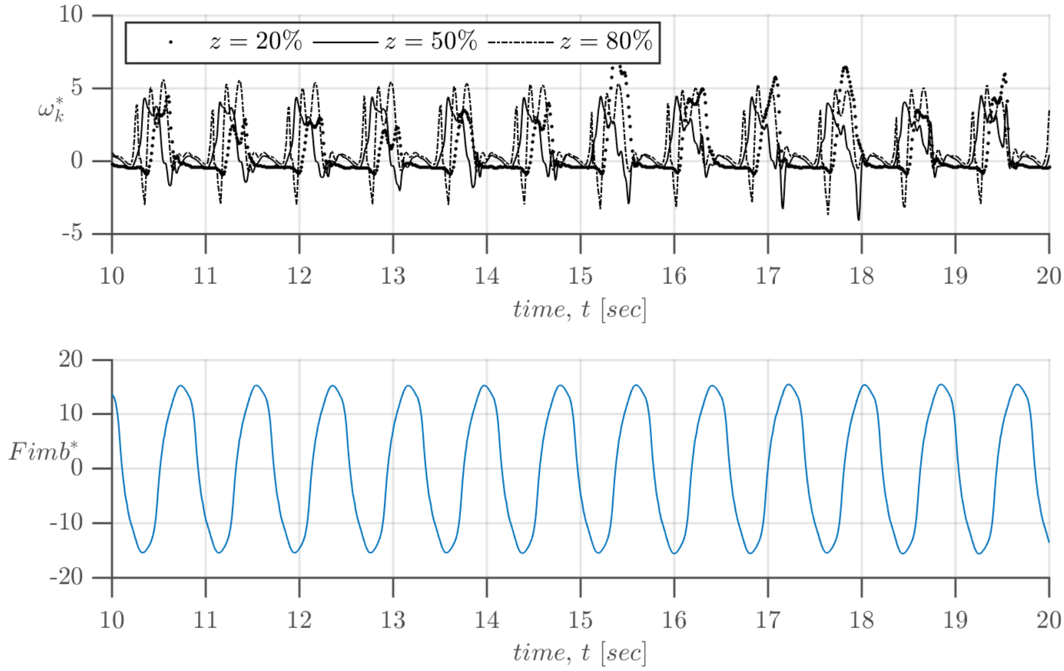

Figure 8: Dimensionless in-plane Vorticity calculated at three monitoring points corresponding to 20, 50 and 80 % of the length of the mast (upper panel) and reduced transversal force vs time (bottom panel)

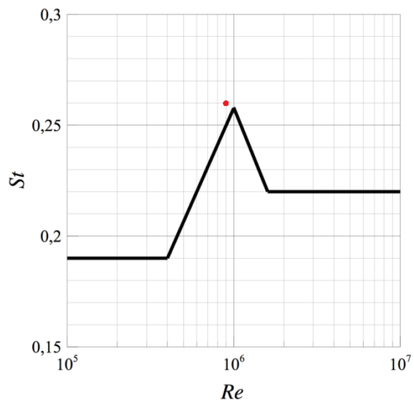

Figure 9: Strouhal number as function of Reynolds number for cylinders, the red dot is the Strouhal number calculated from the simulations.

force calculated at every time step for a generator with the properties of Table 1 connected to a resistive load of $R = 7\,\Omega$. Multiplying these two values (magnet velocity and magnetic force) at every time step, the instant output electrical power is obtained, plotted in the bottom panel together with the instant mechanical power available in the last element of the rod, the latter calculated as expressed in Eq. (46). Both powers are reduced with the power available in the wind Eq. (45), therefore, the plotted data correspond to the mechanical and electrical efficiencies of the VWT. The swept area is calculated knowing the amplitude of the angular displacement, in this simulation, with an angular amplitude of 10 degrees, the swept area is $A_{sw} = 16.23\,m^2$.

$$P_{wind} = 1/2\,\rho\,U^3\,A_{sw} \tag{45}$$

$$P_{mec} = M_{imb,x}\,\omega_x + F_{imb,y}\,v_y \qquad \eta_{mec} = \frac{P_{mec}}{P_{wind}} \tag{46}$$

$$\eta^* = \frac{P_e}{P_{wind}} \tag{47}$$

Here a peak efficiency of $\eta_{peak} = 0.2019$ is reached, and integrating during the period of the

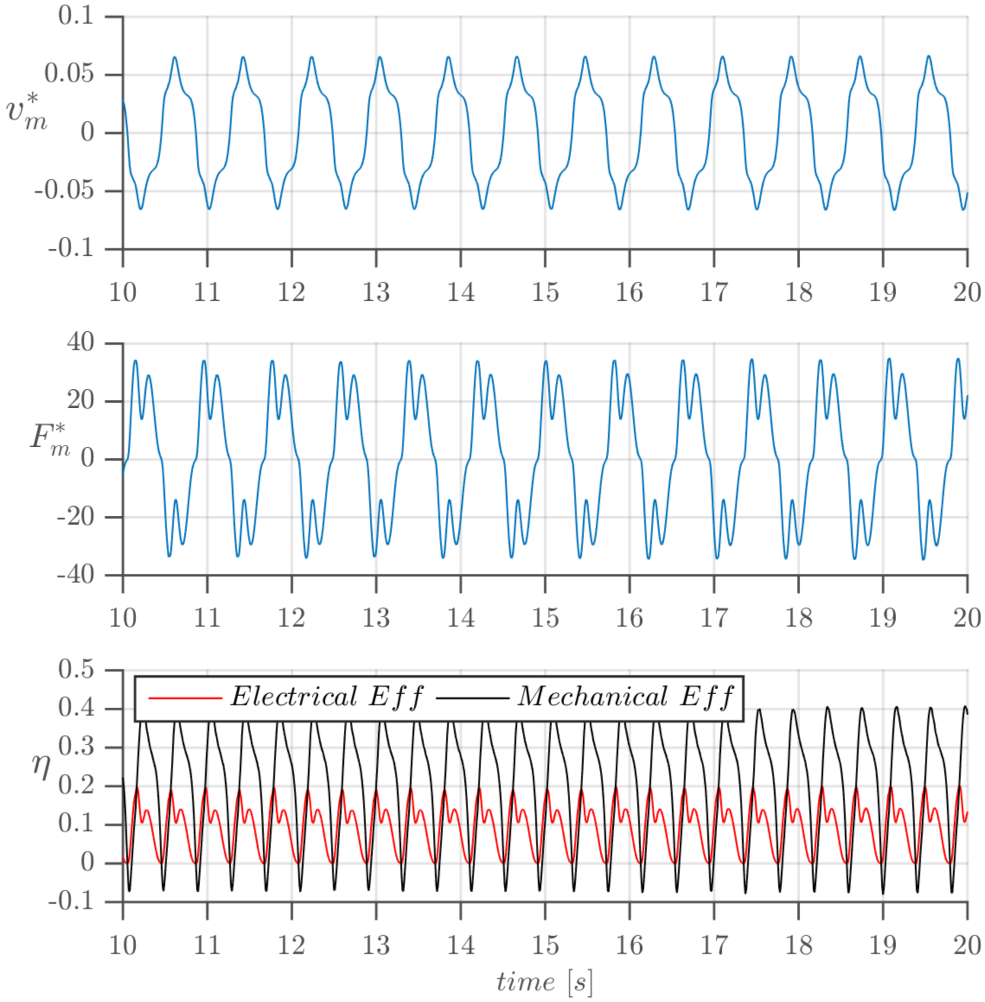

Figure 10: Plot of the magnet velocity (upper panel), magnetic force (mid panel), and instantaneous mechanical and electrical output power (bottom panel), during 10 seconds of simulation with uniform wind velocity of $U_o = 9.1\,m/s$.

simulation and dividing by the time lapse, an integrated efficiency of $\overline{\eta^*} = 0.0944$ is reached.

For a discretized in time system the integrated efficiency is calculated as:

$$\overline{\eta^*} = \frac{1}{N_{steps}\,\Delta t} \sum_{1}^{N_{steps}} \eta^*\,\Delta t \tag{48}$$

The results shown so far, correspond to the same simulation, having a uniform flow velocity of $U_o = 9.1\,m/s$, and two equal resistive loads of $R = 7\,\Omega$ connected at each coil of the generator model. Several simulations where carried out varying alternatively the wind velocity and the resistive load. For each simulation the integrated efficiency was calculated and plotted in Fig. 11 against the wind velocity. The different colors indicate different values of load resistance connected to the coils.

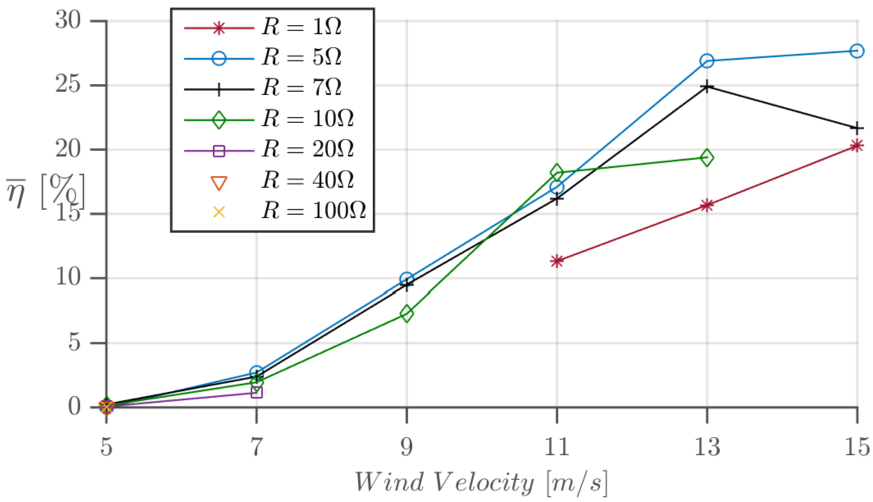

Figure 11: Efficiency vs wind speed parametric in load resistance

The curves presented in Fig. 11 are generally continuous, displaying growing behavior. As the efficiency at low values of wind speed is almost zero, it improves the values for mid wind velocities (shown the horizontal axis), and significantly higher values are reached for higher wind speeds. This is mainly for the structural damping of the rod. For low values of wind velocity, low forces are applied, and so the energy disipated in the material is enough to keep the oscillations within a range of very small amplitude. On the other hand, for high valuess of wind speed the rod adopts large deformations and the amplitude of the oscillations become much wider, reaching higher velocities and forces, hence generating higher values of power. This large deflections on the rod may not be really convenient, as it it may make it prone to malfunction or even risk breaking it, but as the model does not actually implement fracture prediction, it returns high values of output power instead.

4.1 Limitations

The results presented in the previous section describe a VWT adjusted to operate at a wind speed of $v_{wind} = 9.1\,m/s$, seeking to maximize the output power, and thus, the efficiency of the device. However, it was found that at different wind speeds, the same turbine would reach lower values of efficiency. Some chaotic behavior of the structure was found at much higher values of wind speed. This chaos could follow several patterns:

- The frequencies of oscillations are much higher than the frequency of the vortex shedding tabulated for the corresponding Reynolds number,
- The amplitude of the oscillations obtained turned out to be disproportionately big,
- The output power is higher than the power available in the fluid,
- The mechanical power in the rod is higher than the available in the fluid (both are results that actually contradict the laws of thermodynamics).

This phenomenon may be explained because the time step used is not small enough to capture the motion of the mast, hence several cells are crossed by the mast in only one time step, causing erratic and unmeasurable forces over the mast that, when transmitted to the rod, create the illusion of physically unfeasible phenomena. Some testes were carried on, using shorter time steps, but so far the exact combination of time steps (Δt_{dem} and dt) has not been found yet, as it would vary for different values of wind speed.

Anyway, these irregularities could be avoided testing a more damped structure, as it would support larger forces. This can be achieved by changing the entire rod, for instance using a thicker one or changing the properties of the material (i.e using one with higher structural damping), but this is not a functional option, as it would not be actually possible in a real physical setting to change the rod in order to accommodate the system for different wind speeds. A solution that would be both physically feasible and logistically sound would be to implement a variable damping system.

As the model of the generator implemented in these simulations can be interpreted as a damping force in the motion of the rod, by varying the parameters of the generator, the damping of the structure could be measurably modulated. The key is to find a set of parameters for the generator that can maintain the amplitude and velocity of the oscillations within a controlled range while at the same time maximizing the output power. In this case, the resistive load connected to the circuit of the generator would be used to tune the damping, so as to analyze the behavior at different time steps. Equations (38) and (39) explain the inversely proportional relation between the magnetic force (damping) and the value of the load resistance. There is available technology that could, after measuring the wind speed, automate the adjustment of the damping to optimize the power generation under each specific wind conditions.

5 CONCLUSIONS AND FUTURE WORK

The main objective of the present research was to understand, through the use of mathematical models, the potential efficiency of a vorticity wind turbine. In the process of devising the tools to achieve that goal, a three-dimensional numerical method had to be developed for coupling the finite volume and discrete element methods in the analysis of flexible and elastic structures.

For the modeling of the VWT, bending moment transmission was incorporated to the already developed DEM applied to the fish net in a previous work Sassi et al. (2017), whereas the elements of the fishnet are loose ropes, so there is no bending moment transmission in between the elements. Another important variation applied to the method was the approach used for integrating the equations of motion. In the case of the fishnet, a fourth order Runge-Kutta was implemented for solving the ordinary differential equations system, while for the VWT a centered finite difference, as the proposed by Ivanov (2001), was used for the integration. It would be interesting, in order to improve the computational efficiency of the simulation, to incorporate a higher order method, such as the one used in Sassi et al. (2017), or even to consider the incorporation of an adaptive time step, a potential future development that was beyond the scope of this research.

The three-dimensional coupled method for elastic and flexible structures seems to represent qualitatively well the dynamics of the VWT. The frequency of the oscillation (f) is practically the same to the vortex shedding frequency (f_{vs}), managing to capture the lock-in effect. And the vortex shedding frequency is similar to the frequency calculated from the Strouhal number (St), tabulated for cylinders as a function of the Reynolds Number.

Although the displacement of the device is well captured for the transversal direction, it has to be taken into consideration that the study does not involve all the parameters of a real situation, as in this simulation the force in the along wind direction would not be transmitted to the rod, because the measurement of the displacement in this direction is not considered relevant for the study. Drag forces acting over the mast are quantitatively important, and they would produce larger displacements in the stream-wise direction, this effect has not been studied in this research. With respect to this, is worth clarifying that the modeling of the generator that has been implemented is rather simple and performs well for linear displacements only. If the aim was to harvest energy from displacements in every direction, then other kind of power take off system should be considered, for instance a joystick-type generator that could generate with any angular displacement.

Anyway, the simulation for the implemented generator performs quantitatively well, with values that are comparable in terms of peak and integrated efficiencies to the ones presented by Bernitsas et al. (2008b,a) in experimental physical tests for the VIVACE generator. Even taking into consideration that, at least in the simulation stage, the vorticity turbines is less efficient than current blade turbines, the practicality of the method in terms of cost, simplicity of the installation, maintenance and affordability of updates and enhancements, makes it a convenient and scalable solution that could complement rather well other conventional means.

It should also be said that the conical shape of the mast was designed as a means to achieve a perfect synchronization of the vortex shedding all along the mast. Considering that the wind velocity increases with height in the atmospheric boundary layer, the diameter of the oscillating structure should also increase with height to favor the synchronization. In this research, only uniform flows have been tested, but it would be very enriching to simulate the efficiency of this devices under the dynamics of an atmospheric boundary layer. Also further research would allow to determine the most efficient shape for the mast to optimize the synchronization and therefore maximize the output power. Nevertheless, the lock in effect was well captured in the simulations, and synchronization was roughly achieved for the uniform flow. But there is plenty of room for increasing accuracy in upcoming studies looking at the same technology, incorporating new variables and more precise models, and obtaining more predictive simulations.

It is worth mentioning the potential of the method to predict output power for this type of systems, because the ability to test different designs or types of applications would be easily implemented just by introducing the corresponding changes in the code. For instance, those incorporations could allow testing a more sophisticated power take off system or even considering the adaptation of the device to produce energy underwater, harvesting the motion of waves and currents.

ACKNOWLEDGEMENTS

We would like to thanks the support from CAP (*Comision Academica de Posgrado*) and CSIC (*Comision Sectorial de Investigacion Cientifica*), both from the University of the Republic, Motevideo, Uruguay.

REFERENCES

Advisory Committee on Technical Recommendations for Construction, 2010. Guide for the assessment of wind actions and effects on structures. *National Research Council of Rome, Italy*.

Barrero-Gil, A., Pindado, S., & Avila, S., 2012. Extracting energy from vortex-induced vibrations: A parametric study. *Applied Mathematical Modelling*, v. 36, n.1, p. 3153-3160

Bearman, P., 2011. Circular cylinder wakes and vortex-induced vibrations. *Journal of Fluids and Structures*, v. 27, n.1, p. 648-658

Bernitsas, M., Ben-Simon, Y., Raghavan, K., and Garcia, E., 2008a. The vivace converter: model tests at high damping and reynolds number 10^5. *Journal of Offshore Mechanics and Arctic Engineering*, 130(1):1–15.

Bernitsas, M., Raghavan, K., Ben-Simon, Y., and Garcia, E., 2008b. Vivace (vortex induced vibration aquatic clean energy): a new concept in generation of clean and renewable energy from fluid flow. *Journal of Offshore Mechanics and Arctic Engineering*, 130(1):1–15.

Cajas, J., Houzeaux, G., Yez, D., and Mier-Torrecilla, M., 2016. Shape project vortex bladeless: Parallel multi-code coupling for fluid structure interaction in wind energy generation. *Partnership for Advanced Computing in Europe*.

Cundall, P. and Strack, O., 1979. A discrete numerical model for granular assemblies. *Geotechnique*, 29(1):47–65.

Donoso, G., Ladera, C., and Martin, P., 2010. Magnetically coupled magnet-spring oscillators. *European Journal of Physics*, 31(1):433–452.

Fadlun, E., Verzicco, R., Orlandi, P., and Mohd-Yusof, 2000. Combined immersed-boundary finite-difference methods for three-dimensional complex flow simulations. *Journal of Computational Physics*, 161:35–60.

Ferziger, J. H. and Peric, M., 2002. *Computational Methods for Fluid Dynamics*. Springer-Verlag Berlin Heidelberg New York, Germany.

Govardhan, R. and Williamson, C., 2006. Defining the 'modified griffin plot' in vortex-induced vibration: revealing the effect of reynolds number using controlled damping. *Journal of Fluid Mechanics*, 561(1):147–180.

Griffin, O. M., Skop, R. A., and Ramberg, S. E., 1975. The resonant, vortex-exited vibrations of structures and cables systems. *Offshore Technology Conference*, 7(1).

Hockney, R. W. and Eastwood, J. W., 1988. *Computing Simulation Using Particles*. IOP.

Ivanov, R. I., 2001. *Analysis of Structures by the Three Dimensional Discrete Element Method*. Doctor of philosophy, University of Kobe, Japan.

Klamo, J. T., Leonard, A., and Roshko, A., 2005. On the maximum amplitude for a freely vibrating cylinder in crossflow. *Journal of Fluid Mechanics*, 363(1):97–114.

Lange, C. F., Schfer, M., and Durst, F., 2002. Local block refinement with a multigrid flow solver. *International Journal for Numerical Methods in Fluids*, 38(1):21 – 41.

Lehnhuser, T. and Schfer, M., 2002. Improved linear interpolation practice for finite-volume schemes on complex grids. *International Journal for Numerical Methods in Fluids*, 38(7):625 – 645.

Lehnhuser, T. and Schfer, M., 2003. Eficient discretization of pressure-correction equations on non-orthogonal grids. *International Journal for Numerical Methods in Fluids*, 42(2):211 – 231.

Liao, C.-C., Chang, Y.-W., Lin, C.-A., and McDonough, J., 2010. Simulating flows with moving rigid boundary using immersed-boundary method. *International Journal for Numerical Methods in Fluids*, 39(1):152 – 167.

Lilek, Z., Muzaferija, S., Peric, M., and Seidl, V., 1997. An implicit finite-volume method using nonmatching blocks of structured grid. *Numerical Heat Transfer, Part B: Fundamentals*, 32(4):385 – 401.

Mendina, M., Draper, M., Soares, A. P. K., Narancio, G., and Usera, G., 2014. A general purpose parallel block structured open source incompressible flow solver. *Cluster Computing*, 17(2):231 – 241.

Mittal, R. and Iaccarino, G., 2005a. Immersed boundary methods. *Annual Review of Fluid Mechanics*, 37(1):239 – 261.

Mittal, R. and Iaccarino, G., 2005b. Immersed boundary methods. *Annu. Rev. Fluid Mech.*, 37:239–261.

Mohd-Yusof, J., 1998. Development of immersed boundary methods for complex geometries. *Center of Turbulence Research*, Annual Research Briefs:325–336.

Parkinson, G. V., 1972. Mathematical models of flow-induced vibrations of bluff bodies. In *Flow-Induced Structural Vibrations - IUTAM-IAHR Symposium Karlsruhe*, pages 81–127, Berlin.

Peskin, C. S., 1972. Flow patterns around heart valves: A numerical method. *Journal of Computational Physics*, 10:252–271.

Peskin, C. S., 1982. The fluid dynamics of heart valves: Experimental, theoretical and computational methods. *Annual Review of Fluid Mechanics*, 14(2):235.

Peskin, C. S., 2002. The immersed boundary method. *Acta Numerica*, pages 479–517.

Sassi, P., Freira, J., Paz, P. L., Mendina, M., Draper, M., and Usera, G., 2017. Coupled discrete element and finite volume methods for simulating loaded elastic fishnets in interaction with fluid. *Journal of Computers and Fluids*, 156:200–208.

Smagorinsky, J., 1963. General circulation experiments with the primitive equations. *Monthly Weather Review*, 91(3):99 – 164.

Soti, A. K., Thompson, M. C., Sheridan, J., and Bhardwaj, R., 2017. Harnessing electrical power from a vortex-induced vibration of a circular cylinder. *Journal of Fluids and Structures*, 70(1):360–373.

Usera, G., Vernet, A., and Ferr, J. A., 2006. Use of time resolved piv for validating les/dns of the turbulent flow within a pcb enclosure model. *Flow, Turbulence and Combustion*, 77(1):77 – 95.

Usera, G., Vernet, A., and Ferr, J. A., 2008. A parallel block-structured finite volume method for flows in complex geometry with sliding interfaces. *Flow, Turbulence and Combustion*, 81(3):471.

Williamson, C. H. K. and Govardhan, R., 2008. A brief review of recent results in vortex-induced vibrations. *Journal of Wind Engineering and Industrial Aerodynamics*, 96(1):713–135.

Zaleski, S., 2001. Science and fluid dynamics should have more open sources. *online*.